Inorganic Chemistry

pubs.acs.org/IC Article

Abrupt Spin Transition in a Heteroleptic Fe(II) Complex with Pendant Naphthalene Functionality

Sandugash Yergeshbayeva, Jeremy J. Hrudka, Minyoung Jo, Miguel Gakiya-Teruya, Mark W. Meisel, and Michael Shatruk*



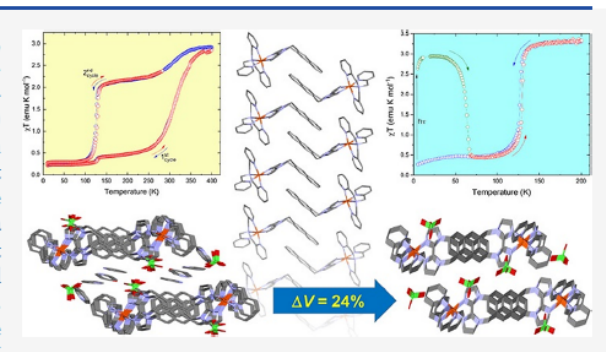


Article Recommendations

ABSTRACT: A heteroleptic spin-crossover (SCO) complex, [Fe(tpma)(xnap-bim)](ClO₄)₂ (1; tpma = tris(2-pyridylmethyl)-amine, xnap-bim = 8,15-dihydrodiimidazo[1,2-a:2',1'-c]naphtho-[2,3-f][1,4]diazocine), has been obtained by reacting a Fe(II) precursor salt with tetradentate tpma and bidentate xnap-bim ligands. Depending on crystallization conditions, two different solvates have been obtained, 1·2.25py·0.5H₂O and 1·py. The former readily loses the interstitial solvent to produce either a powder sample of 1 upon filtration or crystals of 1 if the solvent loss is slowed by placing the crystals of 1·2.25py·0.5H₂O in diethyl ether. In contrast, 1·py exhibits higher stability toward solvent loss. The crystal packing of both solvates and of the solvent-free

structure features double columns of [Fe(tpma)(xnap-bim)]2

Metrics & More



Supporting Information

cations formed by efficient $\pi-\pi$ interactions between the pyridyl groups of tpma ligands, as well as by stacks supported by $\pi-\pi$ interactions between interdigitated naphthalene fragments of xnap-bim ligands. While both solvates show a gradual SCO between the high-spin (HS) and low-spin (LS) states of the Fe(II) ion, solvent-free complex 1 exhibits an abrupt spin transition centered at 127 K, with a narrow 2 K thermal hysteresis. Complex 1 also shows a light-induced excited spin state trapping effect, manifested as LS \rightarrow HS conversion upon irradiation with white light at 5 K. The metastable HS state relaxes to the ground LS state when heated above 65 K.

■ INTRODUCTION

ACCESS I

Transition metal complexes that exhibit switching between high-spin (HS) and low-spin (LS) electronic configurations, generally known as spin crossover (SCO), are of interest for the design of stimuli-responsive materials and devices. 1,2 The drastic differences between structural, optical, magnetic, and dielectric properties of the HS and LS states allow the use of temperature, pressure, or irradiation to achieve the switching behavior.3 Especially appealing are SCO materials that exhibit hysteretic spin-state switching since they offer a range of the parameter space in which the HS and LS states can co-exist and, thus, interconvert due to the action of one of the aforementioned external stimuli.4-14 The emergence of the hysteretic behavior relies on cooperativity, which has been shown to originate from strong vibronic coupling between the metal centers that undergo the SCO. 15-17 Such coupling can be enhanced by providing efficient covalent, 9,18 coordination, $^{19-23}$ hydrogen-bonding, 24,25 and $\pi-\pi$ stacking $^{26-28}$ interactions between coordination spheres of nearest-neighbor SCO metal ions.

A few years ago, our group reported the synthesis of heteroleptic SCO complexes $[Fe^{II}(tpma)(L_2)](ClO_4)_2$, where tpma = tris(2-pyridylmethyl)amine and $L_2 = a$ bidentate ligand

based on 2,2'-biimidazole (bim; Scheme 1).26 While the original complex, [Fe^{II}(tpma)(bim)](ClO₄)₂, showed a gradual SCO centered at $T_{1/2} \sim 190$ K, its derivative, [Fe^{II}(tpma)-(xbim)](ClO₄)₂ (xbim = 1,1'-(α , α '- σ -xylyl)-2,2'-biimidazole), showed an abrupt and hysteretic spin transition at $T_{1/2,\downarrow} = 196$ K and $T_{1/2,\uparrow}$ = 203 K in the cooling and warming regimes, respectively. The change in the character of SCO was attributed to the addition of the o-xylyl functionality that afforded the formation of a columnar structure, in which the SCO cations, [Fe^{II}(tpma)(xbim)]²⁺, were efficiently coupled through π - π and σ - π interactions. The stronger cooperativity of SCO in the xbim-containing complex also led to a much more durable kinetically trapped HS state induced by light irradiation of the LS complex at low temperatures (this lightinduced excited spin state trapping is known as the LIESST effect²⁹). Consequently, [Fe^{II}(tpma)(xbim)](ClO₄)₂ was used

Received: May 3, 2022 Published: July 11, 2022





Scheme 1. Ligands Used for the Synthesis of Heteroleptic SCO Complexes

as a precursor to prepare an SCO semiconducting material by co-crystallization of the SCO cation with fractionally charged $TCNQ^{\delta-}$ anions (0 < δ < 1). [Fe $^{II}(tpma)(xbim)]-(TCNQ)_{1.5}(ClO_4)\cdot DMF$ showed a more gradual SCO, without hysteresis, but the LIESST effect was still observed in the hybrid material. 30

To explore how the extension of the aromatic pendant on the N-alkylated bim derivative might affect the crystal packing and SCO behavior of the heteroleptic Fe(II) complex, we set out to alkylate the bim unit with 2,3-dimethylenenaphthalene to obtain a new ligand, 8,15-dihydrodiimidazo[1,2-a:2',1'c]naphtho[2,3-f][1,4]diazocine (xnap-bim in Scheme 1). The conjecture was that the extended π -system of the peripheral naphthalene fragment of xnap-bim, as compared to xbim, might lead to a more robust crystal packing. Thus, it is of interest to examine how this change in the ligand structure impacts both the crystal structure of the complex and the nature of the spin transition, i.e., its abruptness and thermal hysteresis. Herein, we present the synthesis and detailed investigation of structural and magnetic properties of the heteroleptic complex, $[Fe(tpma)(xnap-bim)](ClO_4)_2$ (1). We demonstrate the strong dependence of the SCO behavior on the presence of an interstitial solvent, as well as the robust nature of crystal packing. Remarkably, the material retains its crystallinity even after the loss of interstitial solvent that causes a 24% decrease in the lattice volume. The preservation of the long-range crystalline order and the closer proximity of the cationic Fe(II) complexes in the desolvated structure lead to a cooperative and abrupt spin transition centered around 127 K, as well as to a LIESST effect with an HS → LS relaxation temperature of 65 K.

■ MATERIALS AND METHODS

Synthesis. All reactions were performed in an inert atmosphere using standard Schlenk techniques. Reagents were purchased from Millipore Sigma, except for 2,3-dimethylnaphthalene (Alfa Aesar). All reagents were used as received. Sodium hydride was obtained as a 60% suspension in mineral oil, and the oil was washed off with hexanes (3 × 20 mL) to afford solid NaH that was used in the reaction. Literature procedures were used to prepare tpma, ³¹ bim, ³² and 2,3-bis(bromomethyl)naphthalene. ³³ Anhydrous commercial solvents were additionally purified by passing through a double-stage drying/purification system (Pure Process Technology, Nashua, NH, USA). Elemental analyses were carried out by Atlantic Microlab, Inc. (Norcross, GA, USA).

8,15-Dihydrodiimidazo[1,2-a:2',1'-c]naphtho[2,3-f][1,4]diazocine (xnap-bim). To a solution of NaH (65.2 mg, 2.72 mmol) in anhydrous DMF (4 mL), cooled in an ice bath, was added via cannula a solution of bim (192 mg, 1.43 mmol) in anhydrous DMF (4 mL). The mixture was stirred for 30 min followed by addition of a solution of 2,3-bis(bromomethyl)naphthalene (415 mg, 1.30 mmol) in anhydrous DMF (4 mL). The color quickly changed to yellow. The reaction mixture was allowed to warm to room temperature (r.t.), and stirring was continued for another 12 h. The solvent was removed on the Schlenk line under vacuum. The crude product was washed with distilled water (100 mL), extracted with chloroform (3 × 20 mL), and dried with MgSO₄. The solvent was removed by rotary evaporation to yield a bright-yellow powder (348 mg, 85%). HR-MS (ESI): Calcd. (Found) for H(xnap-bim)⁺ = $(C_{18}H_{15}N_4)^+$: 287.1296 (287.1300). ¹H NMR (CDCl₃), δ, ppm: 7.85 (m, 2H), 7.76 (s, 2H), 7.56 (m, 2H), 7.26 (s, 2H), 7.16 (s, 2H), 5.06 (s, 4H).

[Fe(tpma)(xnap-bim)](ClO₄)₂ (1). A mixture of [Fe(H₂O)₆]-(ClO₄)₂ (90.7 mg, 0.250 mmol) and tpma (72.6 mg, 0.250 mmol) in anhydrous pyridine (5 mL) was stirred for 10 min to yield a darkgreen solution. A solution of xnap-bim (71.6 mg, 0.250 mmol) in anhydrous pyridine (5 mL) was added, and the green suspension was stirred for an additional 4 h, until a wine-red solution was obtained. The solution was concentrated to half a volume under reduced pressure and filtered under an inert atmosphere. The filtrate was layered with toluene and left undisturbed. Needle-shaped red crystals of 1·2·2·5py·0·5H₂O, with the lengths of several millimeters, were collected after 2 days. When filtered and dried under suction, the crystals yielded a yellow powder of desolvated complex 1 in 41.8% (87.1 mg) yield. Elem. Anal.: Calcd. (Found) for FeCl₂O₈C₃₆N₈H₃₂ (1), %: C, 52·00 (51·90), H, 3.88 (3·92), N 13.48 (13.23).

[Fe(tpma)(xnap-bim)](ClO₄)₂-pyridine (1-py). If the aforementioned procedure to obtain 1·2.5py·0.5H₂O was continued with the crystallization tube left undisturbed for 5–7 days, then dark-red blockshaped crystals of 1-py could be harvested from the bottom of the tube. A bulk sample of 1-py could be obtained by mechanical separation of its distinctly shaped crystals from the filtered product mixture under an optical microscope. The crystals of this solvate were sufficiently stable and did not lose crystallinity even after being exposed to air for several days. Elem. Anal.: Calcd. (Found) for FeCl₂O₈C₄₁N₉H₃₇ (1·py): C, 52.56 (52.79), H, 3.94 (3.97), N, 13.28 (13.28).

The crystallization process can be accelerated by quickly mixing the pyridine solution of 1 with toluene and leaving the mixture undisturbed. This procedure results in higher yield of $1\cdot 2.5$ py· $0.5H_2O$, the crystals of which can be collected after 1 day, but if the mixture is left undisturbed for longer times, then crystals of $1\cdot$ py still appear as a byproduct.

Magnetic Measurements. Magnetic properties were measured on polycrystalline samples using a magnetic property measurement system (MPMS-XL, Quantum Design) equipped with a superconducting quantum interference device (SQUID). Direct-current (DC) magnetic susceptibility was measured in an applied field of 1000 Oe in the 5–400 K temperature range, at a cooling/warming rate of 1 or 2 K/min. The data were corrected for temperature-independent paramagnetism (TIP), due to the contribution from the excited states of the d^6 Fe(II) ion, for diamagnetic contribution from a sample holder, and for the intrinsic diamagnetism using tabulated constants.³⁺

Photomagnetic measurements were performed on the MPMS-XL using a homemade fiberoptic sample holder described elsewhere. S A Quartzline tungsten halogen lamp (400–2200 nm) delivering nominally \sim 20 mW/cm² to the sample provided the broadband white light. The sample was cooled to 5 K at 1 K/min while acquiring data in an applied magnetic field of 1000 Oe. Once the desired temperature was reached, the sample was irradiated while the increase in the magnetic signal from the sample was monitored to evaluate the completeness of the LS \rightarrow HS photoconversion (Figure S3). After 7 h, the time-dependent magnetization signal was close to saturation, at which point the irradiation was discontinued, and the

Scheme 2. Two-Step Synthesis of xnap-bim (NBS = N-Bromosuccinimide; bim = 2,2'-Biimidazole; DMF = N,N-Dimethyformamide)

NBS,
$$(PhCO_2)_2$$

CCI₄, reflux, 6 h

92 %

NaH, bim

DMF,0°C \rightarrow rt, 14h

Table 1. Fe-N Bond Lengths and N-Fe-N Bond Angles in the Structures of Complex 1

compound	1·2.25py	-0.5H ₂ O		1 ·py			1
temperature	100 K	230 K	100 K	230 K	295 K	90 K	295 K
$d(\text{Fe-N})_{\text{average}} \text{ Å}^a$	1.996(4) 2.001(4)	2.148(4) 2.117(4)	1.997(1)	2.003(1)	2.053(2)	2.007(3)	2.191(5)
$\Sigma_{90}(N-Fe-N)$, deg ^a	77.70(2) 72.90(2)	111.4(1) 107.5(2)	69.67(6)	71.02(6)	84.24(8)	70.6(1)	118.2(2)
$(N-Fe-N)_{xnap-bim}$, $deg^{a,b}$	79.54(2) 78.71(2)	77.04(2) 75.95(1)	80.02(6)	79.76(6)	78.58(9)	79.70(1)	75.53(2)
Fe ^{II} spin state ^{a,c}	LS LS	~75% HS ~60% HS	LS	LS	~30% HS	LS	HS
volume per f.u., Å ³	1144.65(5)	1190.5(1)	974.18(5)	996.63(8)	1018.6(1)	865.60(5)	912.80(5)

"Two entries for the crystal structure of 1·2.25py·0.5H₂O correspond to the metric parameters calculated for two symmetry-independent Fe centers. "The chelating angle formed by the N-donor atoms of the bidentate xnap-bim ligands." The percentage of the HS state was determined by using the metric parameters of the structures deemed to be fully LS or HS as terminal points.

DC magnetic susceptibility was measured as the sample was heated to 300 K at a rate of 0.3 K/min.

Powder X-ray Diffraction (PXRD). High-resolution PXRD measurements on a powder sample of 1 were performed at 295 and 100 K on beamline 11-BM-B (λ = 0.414582 Å) of the Advanced Photon Source (APS) facility at Argonne National Laboratory. The unit cell parameters were refined with HighScore Plus software.³⁶

Single-Crystal X-ray Diffraction. Single-crystal X-ray diffraction was performed on a Rigaku-Oxford Diffraction Synergy-S diffractometer equipped with a HyPix detector and monochromated Cu-K α and Mo-K α radiation sources. In a typical experiment, a single crystal was suspended in Parabar oil (Hampton Research) and mounted on a cryoloop that was cooled to the desired temperature in a N2 cold stream. The data set was recorded as ω-scans at 0.5° step width and integrated with the CrysAlis software package. 37 An empirical absorption correction was applied based on spherical harmonics as implemented in the SCALE3 ABSPACK algorithm.³⁸ The space group was determined with CrysAlis, and the crystal structure solution and refinement were carried out with SHELX³⁹ using the interface provided by Olex2.⁴⁰ The final refinement was performed with anisotropic atomic displacement parameters for all non-hydrogen atoms, except for some atoms of highly disordered anions or solvent molecules, which, in such cases, were refined isotropically. Full details of crystal structure refinements and the final structural parameters have been deposited with the Cambridge Crystallographic Data Centre (CCDC). The registry numbers and a brief summary of data collection and refinement parameters are provided in Table S1.

RESULTS AND DISCUSSION

Synthesis. The synthesis of xnap-bim was conducted in two steps from commercially available 2,3-dimethylnaphthalene, which was subjected to benzylic bromination to afford 2,3-bis(bromomethyl)naphthalene that was subsequently used for *N*-alkylation of bim to produce xnap-bim in 78% total yield (Scheme 2).

The heteroleptic complex $[Fe(tpma)(xnap-bim)](ClO_4)_2$ (1) was synthesized by reacting $[Fe(H_2O)_6](ClO_4)_2$ with tpma in the 1:1 ratio in pyridine (py) followed by addition of 1 equiv of xnap-bim. A dark-green suspension became a wine-red solution after stirring for 4 h, and then, crystallization was

induced by layering toluene on top of the pyridine solution. Long red needle-shaped crystals of 1.2.25py.0.5H₂O appeared near the interface between the solvents after 1 day. Upon removal from the mother liquid, 1.2.25py.0.5H2O rapidly lost the solvent and converted to a solvent-free yellow powder of 1, as indicated by thermogravimetric analysis (TGA) shown in Figure S1a. However, if the crystallization tube was left undisturbed for 5-7 days, then darker block-shaped crystals of 1.py appeared in the bottom of the tube. After removal from the mother liquid, these crystals remained stable and did not lose the interstitial solvent for a prolonged period of time, preserving crystallinity even after 1-2 months. TGA performed on these crystals showed that the sample loses ~6.5% of its mass by 154 °C (Figure S1b), which corresponds to a 0.73 pyridine molecule, in a reasonably good agreement with the composition of the solvate established by elemental analysis and X-ray crystallography.

From these observations, we posit that the less stable $1\cdot 2.25 \text{py} \cdot 0.5 \text{H}_2 \text{O}$ is a kinetic product while the more stable $1\cdot \text{py}$ is a thermodynamic product. A pure sample of $1\cdot 2.25 \text{py} \cdot 0.5 \text{H}_2 \text{O}$ could be harvested from the crystallization solution after an initial 1-2 days. On the other hand, crystals of $1\cdot \text{py}$, due to their slower formation, always co-existed with crystals of $1\cdot 2.25 \text{py} \cdot 0.5 \text{H}_2 \text{O}$, even when the crystallization tube was left undisturbed for several months. Therefore, a pure sample of $1\cdot \text{py}$ was obtained by mechanically isolating its distinct block-like crystals from the mixture of products after filtration.

When crystals of $1\cdot 2.25$ py· $0.5H_2O$ were quickly transferred from pyridine to diethyl ether, they converted to desolvated yellow crystals of 1 within 1 h. The crystals of 1 and $1\cdot$ py, as well as the powder of 1 obtained by filtration of $1\cdot 2.25$ py· $0.5H_2O$ in air, are air-stable, but for longer storage, it is recommended to keep them in a desiccator.

Crystal Structures. The crystal structure determination for 1·2.25py·0.5H₂O, 1·py, and 1 was performed at various temperatures to monitor the influence of possible spin-state changes on structural parameters (Table 1). Each crystal

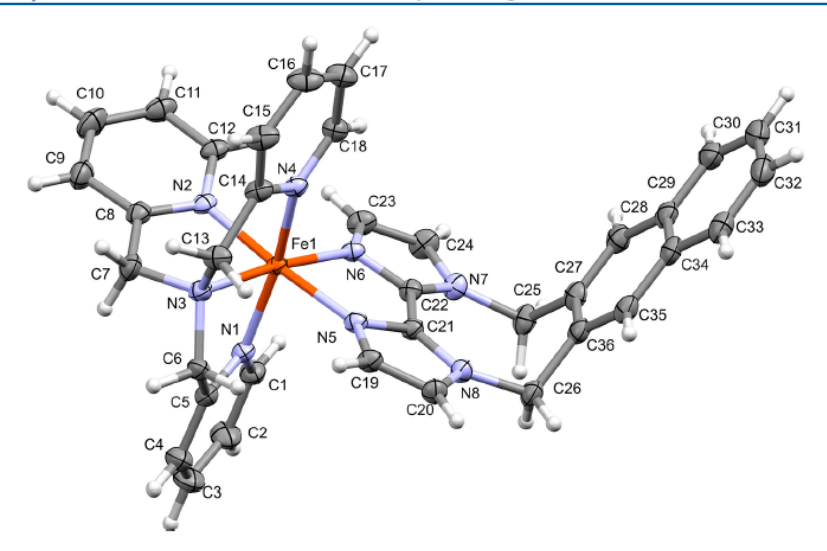


Figure 1. Cation [Fe(tpma)(xnap-bim)]2+ in the crystal structure of 1 at 100 K. Thermal ellipsoids at a 50% probability level.

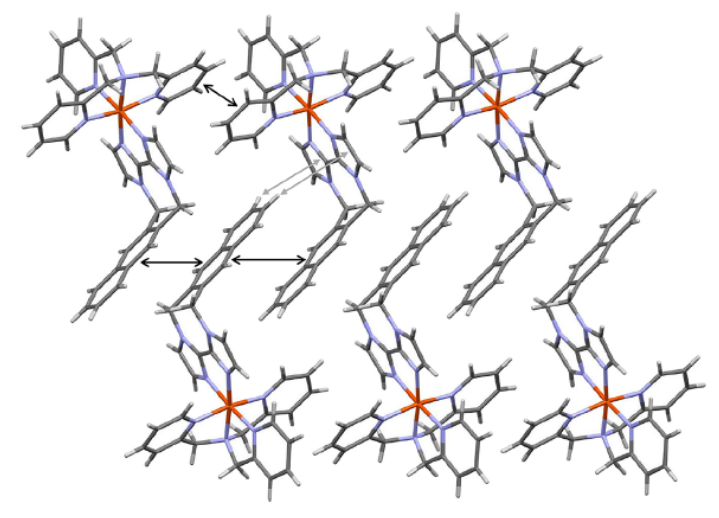


Figure 2. Fragment of the crystal packing of 1-py showing the $[Fe(tpma)(xnap-bim)]^{2+}$ cations arranged in a double column. The $\pi-\pi$ and $\sigma-\pi$ interactions are indicated with black and gray arrows, respectively. See the text for details.

structure contains a mononuclear cationic complex [Fe(tpma)-(xnap-bim)]^{2+} (Figure 1) and accompanying ClO_4^- counter ions, with interstitial solvent molecules also present in the structures of 1·2.25py·0.5H₂O and 1·py. The Fe^{II} ion resides in a distorted octahedral environment of the tetradentate tpma and bidentate xnap-bim ligands. The extent of distortion (Σ_{90}) was quantified by summing the absolute values of deviations of the 12 cis-(N–Fe–N) angles from an ideal value of 90°. It is well established that the HS state typically exhibits longer Fe–ligand bond lengths and larger values of Σ_{90} than those of the LS state. 41,42

The complex $1\cdot 2.25 \text{py} \cdot 0.5 \text{H}_2 \text{O}$ crystallizes in the triclinic space group $P\overline{1}$. The asymmetric unit (a.s.u.) contains two $[\text{Fe}(\text{tpma})(\text{xnap-bim})]^{2+}$ cations, four ClO_4^- anions, four and a half molecules of pyridine, and one molecule of water. The average Fe–N bond length at 100 K is typical of values observed for the LS Fe^{II} ion 41 and well comparable to the

values reported for the parent complexes, [Fe(tpma)(bim)]- $(\text{ClO}_4)_2$ and [Fe(tpma)(xbim)]($(\text{ClO}_4)_2$ (2.022 Å for both). At 230 K, however, the Fe–N bonds become notably longer and the angular distortion of the coordination environment increases substantially (Table 1), indicating a partial conversion to the HS state. One of the symmetry-independent Fe sites shows a slightly larger change toward the HS state than the other site. The comparison to the bond lengths observed in the LS and HS states of 1 (see below) suggests that, at 230 K, the fraction of the HS state in the crystal of $1\cdot 2.25$ py·0.5H₂O is $\sim 75\%$ for the Fe(1) site and $\sim 60\%$ for the Fe(2) site, giving an average HS fraction of 67.5%. The crystal structure determination at room temperature (r.t.) was not possible due to the rapid loss of interstitial solvent that led to the deterioration of crystals of $1\cdot 2.25$ py·0.5H₂O.

The higher stability of 1 py allowed crystal structure determination at 100, 230, and 295 K. At all temperatures,

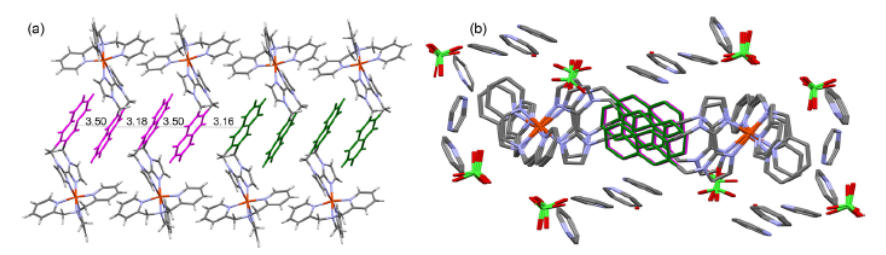


Figure 3. Side (a) and top (b) views of one double column in the crystal structure of $1\cdot 2\cdot 25$ py·0.5H $_2$ O. The naphthalene fragments of two adjacent tetrads are emphasized with different colors. The interplanar distances between naphthalenes are also shown. For clarity, surrounding solvent molecules and anions are omitted in panel (a), and the H atoms are omitted in panel (b). Color scheme: Fe = orange, Cl = green, O = red, N = blue, C = gray.

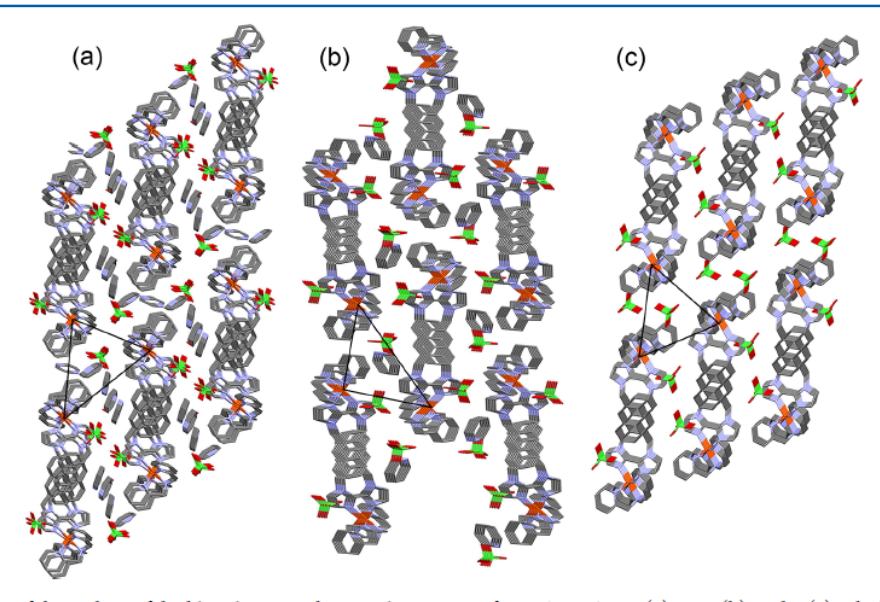


Figure 4. Top view of the packing of double columns in the crystal structures of $1\cdot 2.25py\cdot 0.5H_2O$ (a), $1\cdot py$ (b), and 1 (c). The black lines indicate the shortest intercolumnar distances between Fe centers. These distances are listed in Table 2.

the complex crystallizes in the monoclinic space group P21/c, with the a.s.u. containing one [Fe(tpma)(xnap-bim)]2+ cation, two ClO₄ anions, and one pyridine molecule. At the lowest temperature, the Fe-N bond lengths and the Σ_{90} parameter (Table 1) are comparable to those observed for 1·2.25py-0.5H2O at 100 K, indicating the LS state of the FeII ion. While these parameters remain nearly the same at 230 K, they obviously increase at 295 K, signifying a partial conversion to the HS state. From these metric parameters, we estimate that 1.py contains ~30% of the HS state at 295 K. Even at this temperature, the Fe-N bond lengths and the angular distortion observed in the structure of 1-py are smaller than those observed in the structure of 1.2.25py.0.5H2O at 230 K. These observations suggest that the SCO temperature of 1-py is higher than that of 1.2.25py.0.5H2O, i.e., the relative stability of the LS state in 1.py is increased.

The crystal structure of the desolvated complex 1 was determined at 90 and 295 K. The complex crystallizes in the triclinic space group $P\overline{1}$ at both temperatures. The a.s.u. contains a single $[Fe(tpma)(xnap-bim)]^{2+}$ cation and two ClO_4^- anions. The metric parameters clearly reveal the existence of the Fe^{II} ion in the fully LS state at 90 K and the fully HS state at 295 K (Table 1). Indeed, the room-

temperature structure of 1 shows an average Fe–N bond length of 2.191(5), which is comparable to the value observed in the HS structure of [Fe(tpma)(xbim)](ClO₄)₂ (2.184 Å at 210 K), although the slightly shorter Fe–N bond lengths in the latter can be explained by the lower crystal structure determination temperature. 26

Despite the differences in the a.s.u. content and the space group symmetry, the crystal packing of all three complexes reveals a common feature. The $[Fe(tpma)(xnap-bim)]^{2+}$ cations pack into a double column held together by efficient $\pi-\pi$ interactions between the pyridyl groups of the tpma ligands of adjacent complexes. This packing is also supported by $\pi-\pi$ interdigitation of the pendant naphthalene functionalities of the xnap-bim ligands and weaker $\sigma-\pi$ contacts between the H atoms of the naphthalene fragments and imidazole rings of the xnap-bim ligands (Figure 2). A similar crystal packing motif was observed in the crystal structure of $[Fe(tpma)(xbim)](ClO_4)_2.^{26}$

Nevertheless, the variation in the interstitial solvent content also results in some notable differences in the crystal packing. The stacking of the cations in the double columns appears to be the least regular in the crystal structure of $1\cdot2.25$ py $\cdot0.5H_2$ O. The cations form centrosymmetric tetrads (Figure 3), within

Table 2. Representative Fe···Fe Distances in the Structures of Complex 1

compound	1-2.25py	·0.5H ₂ O		1 ·py		1	
temperature	100 K	230 K	100 K	230 K	295 K	90 K	295 K
d(Fe···Fe), Å							
along the column	9.0954(9)	9.1064(9)	9.1146(6)	9.1637(7)	9.2127(8)	8.8915(7)	9.050(1)
	8.8077(9)	8.9981(9)					
across the column (along the naphthalene units)	14.717(1)	14.809(1)	14.9198(9)	14.990(1)	15.071(1)	14.4385(8)	14.439(2)
	15.672(1)	15.917(1)					
between columns (shortest distances, as shown in	9.5137(9)	10.199(1)	9.3842(8)	9.4973(9)	9.700(1)	9.2941(7)	9.431(2)
Figure 4)	12.214(1)	12.618(1)	9.6970(6)	9.7819(6)	9.8028(6)	9.6657(7)	10.096(1)
	13.008(1)	13.108(1)	13.9266(8)	14.0384(9)	14.187(1)	10.1115(7)	10.477(1)

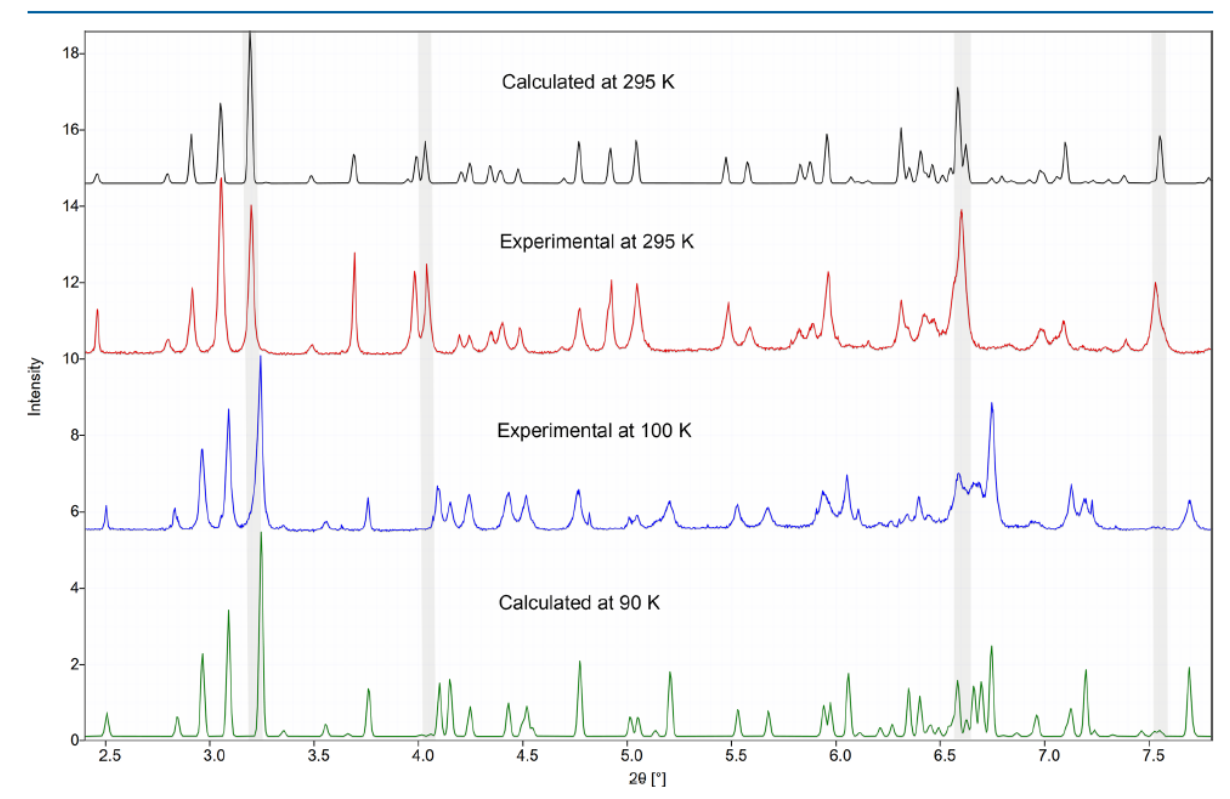


Figure 5. Powder X-ray diffraction patterns of 1 recorded at 295 and 100 K in comparison to the patterns of the HS and LS phase calculated form the crystal structures determined at 295 and 90 K. The gray vertical bands are used to highlight some peaks showing distinct shifts between the HS and LS patterns.

which the interplanar distances between the naphthalene fragments are 3.50, 3.18, and 3.50 Å (at 100 K). The distance between the naphthalene planes of the adjacent tetrads is 3.16 Å. The shorter interplanar distances in the middle of the tetrad and between the tetrads are due to the slippage of the naphthalene planes in the direction perpendicular to the stack propagation and along the shorter side of the naphthalene moieties. Indeed, the naphthalene centroid-to-centroid distances are 3.79, 5.00, and 3.79 Å within the tetrad and 6.38 Å between the tetrads. Such relatively irregular packing of the SCO cations in 1·2.25py·0.5H2O can be explained by the presence of a large amount of interstitial solvent. Although the solvent molecules and perchlorate anions are situated mainly between the double columns of cations, the extensive van der Waals interactions with the cations, while weak, contribute to the partial disruption of the double column (Figure 3b).

The crystal packing of $1\cdot py$ appears to be more regular. The interplanar distances between naphthalene fragments in $1\cdot py$ exhibit alternating values of 3.37 and 3.41 Å, while the centroid-to-centroid distances alternate between 4.05 and 5.34 Å. The larger centroid-to-centroid distance is caused by a larger offset of molecules along the longer axis of the naphthalene fragment. In the solvent-free structure of 1, the crystal packing is also more regular than that of $1\cdot 2\cdot 2\cdot 5py \cdot 0.5H_2O$. In comparison to the crystal structure of $1\cdot py$, the double columns in the structure of 1 show slightly larger but more similar interplanar distances between naphthalene units, alternating between 3.45 and 3.46 Å. On the other hand, the centroid-to-centroid distances became more dissimilar, alternating between 3.80 and 5.49 Å.

While the large amount of interstitial solvent in the structure of $1\cdot 2.25 \text{py}\cdot 0.5 \text{H}_2\text{O}$ causes larger separation between the

Table 3. Unit Cell Parameters of 1 Determined by Single-Crystal and Powder X-ray Diffraction

X-ray method	single	crystal	powder		
temperature	90 K	295 K	100 K	295 K	
unit cell					
a, Å	8.8915(3)	9.0494(3)	8.89(6)	9.04(4)	
<i>b</i> , Å	9.2941(3)	9.4568(5)	9.28(7)	9.46(4)	
c, A	21.2228(8)	21.6041(8)	21.2(1)	21.58(9)	
α , deg	96.866(3)	82.788(4)	96.86(5)	82.67(4)	
β , deg	96.406(3)	84.436(3)	96.392(9)	84.571(8)	
γ, deg	90.771(3)	89.221(4)	90.89(1)	89.301(7)	
V, A ³	1729.7(1)	1825.6(1)	1729(19)	1823(13)	

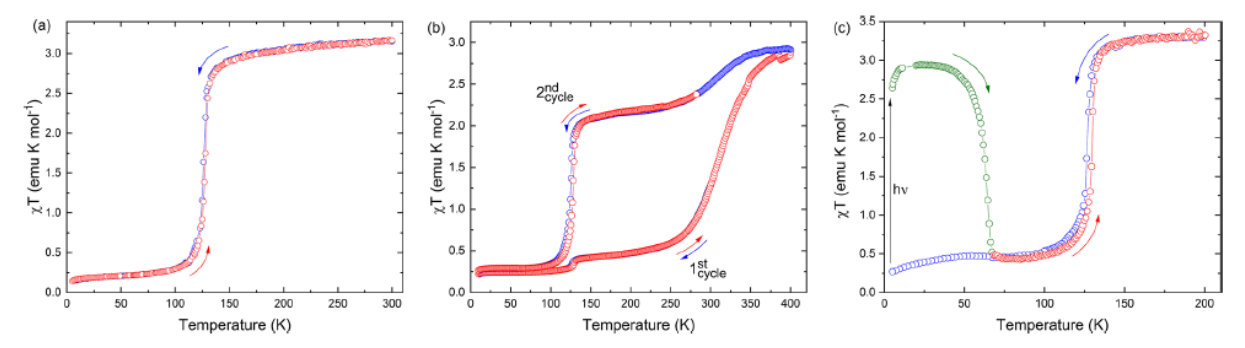


Figure 6. Temperature-dependent χT curves demonstrating (a) an abrupt spin transition with a 2 K thermal hysteresis in a sample of 1 obtained by filtration and drying of 1·2.25py·0.5H₂O, (b) a gradual SCO in a freshly filtered sample of 1·py followed by a more pronounced mixture of the gradual SCO and abrupt spin transition after heating the sample to 400 K in the magnetometer chamber, and (c) the LIESST effect achieved by cooling the sample of 1 to 5 K and irradiating it with white light, after which the sample was heated to room temperature. In all cases, the heating and cooling rates were 1 K/min, with the exception of the LIESST state in panel (c), which was studied in the warming mode at 0.3 K/min.

columns (Figure 4a), in the crystal structure of 1-py, the columns are arranged closer to each other (Figure 4b). The densification of the crystal packing can be also seen from the smaller volume per formula unit (f.u.) in the structure of 1-py as compared to the volume per f.u. in the structure of 1.2.25py. 0.5H₂O (Table 1). Furthermore, in 1·2.25py·0.5H₂O, the solvent molecules are arranged rather loosely in the space between the double columns, which might explain the easy loss of interstitial solvent by this material upon filtration. In contrast, the crystal packing of 1-py reveals that the pyridine molecules are situated between layers of double columns (Figure 4b), and in addition, the perchlorate anions appear to prevent an easy escape of the solvent molecules from the structure. As a result, the solvate remains stable when exposed to air at r.t., and heating to higher temperatures is required for desolvation (Figure S1b).

The crystal packing of 1 (Figure 4c) is also more regular than that of $1\cdot 2\cdot 25 \text{py} \cdot 0.5 \text{H}_2\text{O}$. The interplanar distances between the naphthalene fragments are 3.45 and 3.46 Å, while the centroid-to-centroid distances are 3.80 and 5.49 Å, resembling more the corresponding distances observed in the structure of $1\cdot \text{py}$ rather than in the structure of $1\cdot 2\cdot 25 \text{py} \cdot 0.5 \text{H}_2\text{O}$. Due to the complete loss of interstitial solvent, the volumes per f.u. in the crystal structure of 1 are smaller by 24.4 and 11.1% than the volumes per f.u. in $1\cdot 2\cdot 25 \text{py} \cdot 0.5 \text{H}_2\text{O}$ and $1\cdot \text{py}$, respectively.

The crystal structure of $1 \cdot py$ exhibits slightly different topology of the double-column packing as compared to the crystal structures of $1 \cdot 2.25 py \cdot 0.5 H_2 O$ and 1 (see Figure 4), but the latter two structures can be compared more directly. Table 2 summarizes the shortest Fe···Fe distances along the column

(separated by the interaction between the tpma ligands), across the column (separated by the naphthalene fragments), and between the columns (as defined by black triangles in Figure 4). Due to the more compact structure, the Fe···Fe distances between the columns in 1 are notably shorter than those in $1\cdot 2\cdot 25$ py· $0\cdot 5H_2$ O. The shortest inter-columnar Fe···Fe distances decrease with the decreasing solvent content in the structure.

A comparison of the crystal packings in Figure 4 clearly reveals that there is a straightforward pathway from the crystal structure of 1.2.25py.0.5H2O to that of 1 through desolvation, but a conversion from 1-py to 1 will require a much more substantial displacement of the crystal packing. To explore the desolvation of 1·2.25py·0.5H2O in greater detail, we performed synchrotron high-resolution powder X-ray diffraction (PXRD) on a sample of 1 obtained after filtration of 1.2.25py.0.5H2O in air. The PXRD patterns collected at 295 and 100 K (Figure 5) revealed sharp peaks, confirming that the sample preserves its crystallinity. A clear shift of the 100 K pattern to the higher diffraction angles relative to the 295 K pattern is in agreement with the decrease in the unit cell volume associated with the HS → LS transition. Indeed, the patterns were successfully indexed with the calculated PXRD pattern of 1, giving the unit cell parameters in good agreement with those established from the single-crystal X-ray diffraction (Table 3).

The collapse of the structure upon solvent loss appears to be irreversible. Attempts to re-solvate a sample of 1 by exposing it to pyridine or methanol, or even by immersing crystals in the solvent, did not affect the color of the crystal or the unit cell volume. Apparently, the efficient intermolecular interactions achieved in the desolvated structure contribute to its stability.

Magnetic and Photomagnetic Properties, Magnetic measurements were performed on polycrystalline samples 1-py and 1. The desolvated yellow powder of 1, which was obtained after filtering crystals of 1.2.25py.0.5H2O, showed a χT value of 3.17 emu·K/mol at 300 K. This value is consistent with the spin-only $\chi T = 3.00 \text{ emu-K/mol}$ expected for the HS Fe^{II} ion (S = 2). The slightly higher experimental χT value is explained by orbital contribution to the magnetic moment. 43 Upon cooling at a rate of 1 K/min, the sample showed an abrupt decrease in χT , indicative of a cooperative spin transition (Figure 6a). The transition temperature $(T_{1/2})$, at which the fractions of HS and LS states are equal, was found equal to 126 K upon cooling and 128 K upon warming, thus revealing a 2 K thermal hysteresis. The width of the hysteresis remained the same when the temperature was changed at a rate of 2 K/min. A residual low-temperature χT value of ~ 0.2 emu·K/mol can be explained by a minor fraction of the HS state that might remain on the surface or other defects present in the sample.

A dramatically different magnetic behavior was observed for the solvated sample 1-py. As the sample was cooled from 300 K and then warmed to 400 K (the first cycle in Figure 6b), a gradual and reversible SCO was observed, with $T_{1/2} = 314$ K. A minor anomaly observed as an abrupt spin transition at ~ 127 K suggests that this sample also contained a small amount of the desolvated complex 1. As the sample was cooled from 400 K, the gradual SCO became less pronounced while the abrupt spin transition at lower temperature increased substantially (the second cycle in Figure 6b). This observation can be explained by the solvent loss that leads to the partial conversion of 1-py to 1 at higher temperatures within the magnetometer chamber.

The difference in the magnetic behavior of 1-py and 1 can be attributed to the loss of cooperativity caused by the presence of the interstitial solvent in the former structure. The closer distances between the SCO cations in the solvent-free structure of 1 lead to the cooperative and abrupt spin transition. On the other hand, the $T_{1/2}$ values for the two samples differ by ~200 K, indicating a relatively higher stability of the LS state in 1-py. Such an effect can emerge from the rarger distortion of the coordination environment of Fe^{II} sites in structure 1 due to intermolecular packing forces. 42,44 This assumption could be probed by the analysis of the angular distortion parameter, Σ_{90} , which equals to 69.67(6) and 70.6(1)° for the LS structures of 1-py and 1, respectively (Table 2). The Fe^{II} coordination in 1 appears to be slightly more distorted, but the difference of $\sim 1^{\circ}$ is rather small, taking into account that Σ_{90} is a result of summation over 12 different cis-N-Fe-N angles. Thus, more subtle factors can be at play here, such as electron density redistribution due to the more efficient intermolecular interactions in structure 1.

The abrupt spin transition observed for complex 1 also suggests that this material might exhibit a light-induced excited spin state trapping (LIESST) effect. A thin layer of yellow powder of 1 was irradiated with white light (\sim 20 mW/cm²) in a static magnetic field of 1000 Oe at 5 K, which led to the increase in the observed magnetization. After 7 h, the irradiation source was switched off and the magnetic susceptibility was measured in the warming mode at 0.3 K/min (the green curve in Figure 6c). A χT value at 5 K increased from 0.27 emu·K/mol before irradiation to 2.64 emu·K/mol after irradiation. Upon heating from 5 K, the χT increased to a plateau of \sim 2.95 emu·K/mol at 25 K, suggesting a nearly complete light-induced conversion to the HS state. (The

decrease in χT below 25 K is explained by zero-field splitting effects.) Heating above 50 K led to a rapid decrease in χT due to the relaxation of the metastable HS state to the ground LS state. The fraction of the HS state at 25 K was estimated by assuming that the sample is in the fully HS state at 200 K (Figure 6c). Given that the χT value at 200 K is 3.32 emu·K/mol, the fraction of the light-induced HS state is ~90%. The characteristic temperature, $T_{\rm LIESST}$, was determined to be 65 K from the minimum of the $\partial(\chi T)/\partial T$ curve in the region of the thermally induced HS \rightarrow LS relaxation.

It is interesting to compare the magnetic and photomagnetic properties of 1 to those of the previously reported parent complex, $[\mathrm{Fe}(\mathrm{tpma})(\mathrm{xbim})](\mathrm{ClO_4})_2.^{26}$ Both exhibit abrupt spin transitions with narrow thermal hysteresis. The $T_{1/2}$ for complex 1 is notably lower (126 K upon cooling and 128 K upon warming) than the $T_{1/2}$ for $[\mathrm{Fe}(\mathrm{tpma})(\mathrm{xbim})](\mathrm{ClO_4})_2$ (196 and 203 K, respectively). On the other hand, the T_{LIESST} for 1 (65 K) is higher than the value reported for $[\mathrm{Fe}(\mathrm{tpma})(\mathrm{xbim})](\mathrm{ClO_4})_2$ (52 K). The increase in the T_{LIESST} value might be correlated with the decrease in $T_{1/2}$ for 1 as both effects are in agreement with an increased stability of the HS state relative to the LS state. 11,45

CONCLUSIONS

This work demonstrates the efficacy of the ligand set, composed from tetradentate tpma and N-alkylated bidentate bim, for the preparation of novel SCO complexes. Moreover, the pendant aromatic functionality on the N-alkylated bim promotes efficient columnar stacking of SCO cations, supported by additional intermolecular $\pi-\pi$ interactions between pyridyl groups of tpma. Such crystal packing motif appears to be remarkably robust with respect to the loss of interstitial solvent as the structure sustains a 24% decrease in lattice volume due to solvent loss, without the loss of crystallinity. Moreover, even integrity of single crystals can be preserved if the desolvation is carried out under controlled conditions. While gradual SCO is observed for two different solvated structures of $[Fe(tpma)(xnap-bim)](ClO_4)_2$, the densification of the structure caused by the complete solvent loss results in a material that exhibits an abrupt spin transition. It is of interest to extend this research to other derivatives of bim with extended aromatic pendants, such as anthracene, pyrene, perylene, etc. Such derivatization can lead not only to crystal packings that promote abrupt and hysteretic spin transitions but also to interesting photophysical behavior. Efforts in this direction are currently under way, and their results will be reported in due course.

ASSOCIATED CONTENT

Supporting Information

The Supporting Information is available free of charge at https://pubs.acs.org/doi/10.1021/acs.inorgchem.2c01490.

Thermogravimetric curves, summaries of single-crystal X-ray data collection and crystal structure refinements, fitting of PXRD patterns, the ¹H NMR spectrum of the xnap-bim ligand, and additional data related to photomagnetic studies (PDF).

Accession Codes

CCDC 2169596, 2169599–2169603, and 2169608 contain the supplementary crystallographic data for this paper. These data can be obtained free of charge via www.ccdc.cam.ac.uk/data_request/cif, or by emailing data_request@ccdc.cam.ac.

uk, or by contacting The Cambridge Crystallographic Data Centre, 12 Union Road, Cambridge CB2 1EZ, UK; fax: +44 1223 336033.

AUTHOR INFORMATION

Corresponding Author

Michael Shatruk — Department of Chemistry and Biochemistry, Florida State University, Tallahassee, Florida 32306-4390, United States; orcid.org/0000-0002-2883-4694; Email: shatruk@chem.fsu.edu

Authors

- Sandugash Yergeshbayeva Department of Chemistry and Biochemistry, Florida State University, Tallahassee, Florida 32306-4390, United States
- Jeremy J. Hrudka Department of Chemistry and Biochemistry, Florida State University, Tallahassee, Florida 32306-4390, United States
- Minyoung Jo Department of Chemistry and Biochemistry, Florida State University, Tallahassee, Florida 32306-4390, United States
- Miguel Gakiya-Teruya Department of Chemistry and Biochemistry, Florida State University, Tallahassee, Florida 32306-4390, United States
- Mark W. Meisel Department of Physics, University of Florida, Gainesville, Florida 32611-8440, United States; National High Magnetic Field Laboratory, Gainesville, Florida 32611-8440, United States; orcid.org/0000-0003-4980-5427

Complete contact information is available at: https://pubs.acs.org/10.1021/acs.inorgchem.2c01490

Notes

The authors declare no competing financial interest.

■ ACKNOWLEDGMENTS

This research was supported by the National Science Foundation through awards CHE-1955754 to M.S. and, in part, DMR-170841 (M.W.M.) and DMR-1644779 (National High Magnetic Field Laboratory). S.Y. also acknowledges support from the Chateaubriand Fellowship program. The Rigaku Synergy-S single-crystal X-ray diffractometer used for crystallographic work was acquired through the NSF MRI program (CHE-1828362). This research used resources of the Advanced Photon Source (APS), a U.S. Department of Energy (DOE) Office of Science User Facility operated for the DOE Office of Science by Argonne National Laboratory (ANL) under contract no. DE-AC02-06CH11357. The project also used resources provided by the X-ray Crystallography Center (FSU075000XRAY) and the Materials Characterization Laboratory (FSU075000MAC) at the Department of Chemistry and Biochemistry, Florida State University.

REFERENCES

- (1) Kumar, K. S.; Ruben, M. Sublimable Spin-Crossover Complexes: From Spin-State Switching to Molecular Devices. *Angew. Chem., Int. Ed.* 2021, 60, 7502–7521.
- (2) Molnár, G.; Rat, S.; Salmon, L.; Nicolazzi, W.; Bousseksou, A. Spin Crossover Nanomaterials: From Fundamental Concepts to Devices. *Adv. Mater.* 2018, *30*, 1703862.
- (3) Murray, K. S. The Development of Spin-Crossover Research. In Spin-Crossover Materials: Properties and Applications; Halcrow, M. A., Ed. John Wiley & Sons Ltd.: 2013; pp. 1–54.

- (4) Kahn, O.; Martinez, C. J. Spin-Transition Polymers: From Molecular Materials toward Memory Devices. *Science* 1998, 279, 44–
- (5) Murray, K. S.; Kepert, C. J. Cooperativity in Spin Crossover Systems: Memory, Magnetism and Microporosity. *Top. Curr. Chem.* 2004, 233, 195–228.
- (6) Sato, O. Optically Switchable Molecular Solids: Photoinduced Spin-Crossover, Photochromism, and Photoinduced Magnetization. *Acc. Chem. Res.* 2003, 36, 692–700.
- (7) Weber, B.; Bauer, W.; Obel, J. An Iron(II) Spin-Crossover Complex with a 70 K Wide Thermal Hysteresis Loop. *Angew. Chem., Int. Ed.* 2008, 47, 10098–10101.
- (8) Niel, V.; Thompson, A. L.; Goeta, A. E.; Enachescu, C.; Hauser, A.; Galet, A.; Munoz, M. C.; Real, J. A. Thermal- and Photoinduced Spin-State Switching in an Unprecedented Three-Dimensional Bimetallic Coordination Polymer. Chem. Eur. J. 2005, 11, 2047–2060
- (9) Chakraborty, P.; Bronisz, R.; Besnard, C.; Guénée, L.; Pattison, P.; Hauser, A. Persistent Bidirectional Optical Switching in the 2D High-Spin Polymer {[Fe(bbtr)₃]((BF₄)₂)}_∞. J. Am. Chem. Soc. 2012, 134. 4049–4052.
- (10) Slimani, A.; Varret, F.; Boukheddaden, K.; Garrot, D.; Oubouchou, H.; Kaizaki, S. Velocity of the High-Spin Low-Spin Interface inside the Thermal Hysteresis Loop of a Spin-Crossover Crystal, Via Photothermal Control of the Interface Motion. *Phys. Rev. Lett.* 2013, 110, No. 087208.
- (11) Varret, F.; Boukheddaden, K.; Chastanet, G.; Paradis, N.; Létard, J. F. When T(LIESST) Meets Thermal Hysteresis - a Theoretical Approach. Eur. J. Inorg. Chem. 2013, 763–769.
- (12) Brooker, S. Spin Crossover with Thermal Hysteresis: Practicalities and Lessons Learnt. Chem. Soc. Rev. 2015, 44, 2880–2802
- (13) Shatruk, M.; Phan, H.; Chrisostomo, B. A.; Suleimenova, A. Symmetry-Breaking Structural Phase Transitions in Spin Crossover Complexes. *Coord. Chem. Rev.* 2015, 289, 62–73.
- (14) García-López, V.; Palacios-Corella, M.; Cardona-Serra, S.; Clemente-León, M.; Coronado, E. Spin-Crossover Iron(II) Complex Showing Thermal Hysteresis around Room Temperature with Symmetry Breaking and an Unusually High T(LIESST) of 120 K. Chem. Commun. 2019, 55, 12227–12230.
- (15) Popa, A.-I.; Stoleriu, L.; Enachescu, C. Tutorial on the Elastic Theory of Spin Crossover Materials. J. Appl. Phys. 2021, 129, 131101.
- (16) Nishino, M.; Singh, Y.; Boukheddaden, K.; Miyashita, S. Tutorial on Elastic Interaction Models for Multistep Spin-Crossover Transitions. J. Appl. Phys. 2021, 130, 141102.
- (17) Enachescu, C.; Hauser, A. Study of Switching in Spin Transition Compounds within the Mechanoelastic Model with Realistic Parameters. *Phys. Chem. Chem. Phys.* **2016**, *18*, 20591–20599.
- (18) Chakraborty, P.; Enachescu, C.; Humair, A.; Egger, L.; Delgado, T.; Tissot, A.; Guénée, L.; Besnard, C.; Bronisz, R.; Hauser, A. Light-Induced Spin-State Switching in the Mixed Crystal Series of the 2D Coordination Network {[Zn₁−xFex(bbtr)₃](BF4)₂}∞: Optical Spectroscopy and Cooperative Effects. Dalton Trans. 2014, 43, 17786−17796.
- (19) Coronado, E.; Gimenez-Lopez, M. C.; Levchenko, G.; Romero, F. M.; Garcia-Baonza, V.; Milner, A.; Paz-Pasternak, M. Pressure-Tuning of Magnetism and Linkage Isomerism in Iron(II) Hexacyanochromate. J. Am. Chem. Soc. 2005, 127, 4580–4581.
- (20) Muñoz, M. C.; Real, J. A., Polymeric Spin-Crossover Materials. In Spin-Crossover Materials: Properties and Applications, Halcrow, M. A., Ed. John Wiley & Sons Ltd.: 2013; pp. 121–146.
- (21) Hilfiger, M. G.; Chen, M.; Brinzari, T. V.; Nocera, T. M.; Shatruk, M.; Petasis, D. T.; Musfeldt, J. L.; Achim, C.; Dunbar, K. R. An Unprecedented Charge Transfer Induced Spin Transition in an Fe-Os Cluster. *Angew. Chem., Int. Ed.* 2010, 49, 1410–1413.
- (22) Shimamoto, N.; Ohkoshi, S.; Sato, O.; Hashimoto, K. Control of Charge-Transfer-Induced Spin Transition Temperature on Cobalt-Iron Prussian Blue Analogues. *Inorg. Chem.* 2002, 41, 678–684.

Inorganic Chemistry Article pubs.acs.org/IC

- (23) Avendano, C.; Hilfiger, M. G.; Prosvirin, A.; Sanders, C.; Stepien, D.; Dunbar, K. R. Temperature and Light Induced Bistability in a Co₃[Os(CN)₆]₂·6H₂O Prussian Blue Analog. J. Am. Chem. Soc. 2010, 132, 13123-13125.
- (24) Lian, K.-T.; Wu, W.-W.; Huang, G.-Z.; Liu, Y.; Wu, S.-G.; Ni, Z.-P.; Tong, M.-L. Reversible Step Spin Crossover Modulation Via Water Absorption and Dehydration in a 3d Hofmann-Type Framework. Inorg. Chem. Front. 2021, 8, 4334-4340.
- (25) Zenno, H.; Kobayashi, F.; Nakamura, M.; Sekine, Y.; Lindoy, L. F.; Hayami, S. Hydrogen Bond-Induced Abrupt Spin Crossover Behaviour in 1-D Cobalt(II) Complexes - the Key Role of Solvate Water Molecules. Dalton Trans. 2021, 50, 7843-7853.
- (26) Phan, H. V.; Chakraborty, P.; Chen, M. M.; Calm, Y. M.; Kovnir, K.; Keniley, L. K.; Hoyt, J. M.; Knowles, E. S.; Besnard, C.; Meisel, M. W.; Hauser, A.; Achim, C.; Shatruk, M. Heteroleptic Fe^{II} Complexes of 2,2'-Biimidazole and Its Alkylated Derivatives: Spin-Crossover and Photomagnetic Behavior. Chem. - Eur. J. 2012, 18, 15805-15815.
- (27) Juhász, G.; Hayami, S.; Sato, O.; Maeda, Y. Photo-Induced Spin Transition for Iron(III) Compounds with π - π Interactions. Chem. Phys. Lett. 2002, 364, 164-170.
- (28) Dupouy, G.; Marchivie, M.; Triki, S.; Sala-Pala, J.; Salaün, J. Y.; Gómez-García, C. J.; Guionneau, P. The Key Role of the Intermolecular π - π Interactions in the Presence of Spin Crossover in Neutral $[Fe(abpt)_2A_2]$ Complexes (A = Terminal Monoanion N)Ligand). Inorg. Chem. 2008, 47, 8921-8931.
- (29) Hauser, A. Light-Induced Spin Crossover and the High-Spin → Low-Spin Relaxation. Top. Curr. Chem. 2004, 234, 155-198.
- (30) Phan, H.; Benjamin, S. M.; Steven, E.; Brooks, J. S.; Shatruk, M. Photomagnetic Response in Highly Conductive Iron(II) Spin-Crossover Complexes with Tcnq Radicals. Angew. Chem., Int. Ed. 2015, 54, 823-827.
- (31) Kojima, T.; Leising, R. A.; Yan, S.; Que, L., Jr. Alkane Functionalization at Nonheme Iron Centers. Stoichiometric Transfer of Metal-Bound Ligands to Alkane. J. Am. Chem. Soc. 1993, 115,
- (32) Xiao, J.-C.; Shreeve, J. M. Synthesis of 2,2'-Biimidazolium-Based Ionic Liquids: Use as a New Reaction Medium and Ligand for Palladium-Catalyzed Suzuki Cross-Coupling Reactions. J. Org. Chem. 2005, 70, 3072-3078.
- (33) Chenguang, W.; Mosberg, H. I. Synthesis of a Novel Series of Topographically Constrained Amino Acids: Benzo-1,2,3,4-Tetrahydroisoquinoline-3-Carboxylic Acids. Tetrahedron Lett. 1995, 36, 3623-3626.
- (34) Bain, G. A.; Berry, J. F. Diamagnetic Corrections and Pascal's Constants. J. Chem. Educ. 2008, 85, 532-536.
- (35) Knowles, E. S. Strain-Mediated Photomagnetic Effects in Heterostructured Nanoparticles of Prussian Blue Analogues; Ph.D. Thesis, University of Florida, Gainesville, FL, 2013.
- (36) X'Pert Highscore Plus Software V. 2.2b; PANalytical B.V.: Almelo, Netherlands, 2006.
- (37) CrysAlis; Oxford Diffraction Ltd.: Abingdon, England, 2006.
- (38) Scale 3 Abspack an Oxford Diffraction Program (1.0.4,GUI:1.0.3); Oxford Diffraction Ltd.: Abingdon, England, 2005.
- (39) Sheldrick, G. M. Crystal Structure Refinement with SHELXL. Acta Crystallogr. Sect. C: Struct. Chem. 2015, 71, 3-8.
- (40) Dolomanov, O. V.; Bourhis, L. J.; Gildea, R. J.; Howard, J. A. K.; Puschmann, H. Olex2: A Complete Structure Solution, Refinement and Analysis Program. J. Appl. Crystallogr. 2009, 42, 339-341.
- (41) Guionneau, P.; Marchivie, M.; Bravic, G.; Létard, J. F.; Chasseau, D. Structural Aspects of Spin Crossover. Example of the [Fe^{II}L_n(NCS)₂] Complexes. Top. Curr. Chem. 2004, 234, 97-128.
- (42) Phan, H.; Hrudka, J. J.; Igimbayeva, D.; Lawson Daku, L. M.; Shatruk, M. A Simple Approach for Predicting the Spin State of Homoleptic Fe(II) Tris-Diimine Complexes. J. Am. Chem. Soc. 2017, 139, 6437-6447.
- (43) Shatruk, M.; Dragulescu-Andrasi, A.; Chambers, K. E.; Stoian, S. A.; Bominaar, E. L.; Achim, C.; Dunbar, K. R. Properties of Prussian Blue Materials Manifested in Molecular Complexes:

- Observation of Cyanide Linkage Isomerism and Spin-Crossover Behavior in Pentanuclear Cyanide Clusters. J. Am. Chem. Soc. 2007, 129, 6104-6116,
- (44) Hrudka, J. J.; Phan, H.; Lengyel, J.; Rogachev, A. Y.; Shatruk, M. Power of Three: Incremental Increase in the Ligand Field Strength of N-Alkylated 2,2'-Biimidazoles Leads to Spin Crossover in Homoleptic Tris-Chelated Fe(II) Complexes. Inorg. Chem. 2018, 57, 5183-5193.
- (45) Létard, J. F. Photomagnetism of Iron(II) Spin Crossover Complexes-the T(LIESST) Approach. J. Mater. Chem. 2006, 16, 2550-2559.